Spatial distribution of coherent structures in a self-similar axisymmetric turbulent wake

Weijun Yin,[1] Shancong Tao,[1] Koji Nagata,[2] Yasumasa Ito,[3] Yasuhiko Sakai,[4] and Yi Zhou[1,*]

[1]*School of Energy and Power Engineering, Nanjing University of Science and Technology, Nanjing 210094, China*

[2]*Department of Mechanical Engineering and Science, Kyoto University, Kyoto 615-8540, Japan*

[3]*Graduate School of Engineering, Nagoya University, Nagoya 464-8603, Japan*

[4]*Nagoya Industrial Science Research Institute, Yotsuya-Dori 1-13, Chikusa-ku, Nagoya 464-0819, Japan*

(Received 10 October 2022; accepted 8 August 2023; published 24 August 2023)

The coherent structures play a significantly important role in the spatial evolution of turbulent wakes. The spatial distribution and the organization of the coherent structures in a self-similar axisymmetric turbulent wake are numerically discussed by using the data from the previous simulation [Zhou and Vassilicos, Related self-similar statistics of the turbulent/non-turbulent interface and the turbulence dissipation, J. Fluid Mech. **821**, 440 (2017).], in which it was found that the radial positions of the turbulent/nonturbulent (T/NT) interface at different downstream locations exhibits a self-similar form normalized by the wake width δ. The Liutex method is used to automatically identify the vortex core center and compute the direction of the vortex axis. The probability density functions (PDFs) of the radial distance of the vortex core center R_c at different streamwise locations can be superimposed on the same curve, and the PDFs of R_c scale with δ. There is a discernible preference for the vortex axis to be normal to the mean direction of the flow, and the PDFs of the polar angle α at different downstream locations collapse onto a single curve. The PDFs of the separation distance R_{ct} between the T/NT interface and the nearest vortex core center are also self-similar and scale with δ. The averaged radial distance $\overline{R_{ct}}$ is of the order of the Taylor microscale. The results reported in this work suggest that the coherent structures are orderly distributed and also regularly organized in a self-similar axisymmetric turbulent wake.

DOI: 10.1103/PhysRevFluids.8.084603

I. INTRODUCTION

According to Townsend's hypothesis, all free-shear flows eventually will possess turbulence statistics exhibiting a self-similar profile [1]. Self-similarity is an important concept for the investigation of turbulent shear flows. More specifically, self-similarity here refers to the fact that for a free-shear flow, the statistical distributions of a one-point statistic at different downstream locations can be superimposed on the same curve when normalized by the corresponding local statistical parameters. Consider, for instance the case of an axisymmetric turbulent wake. The mean streamwise velocity $U(x, r)$ is a function of the streamwise distance x and the radial distance r. The mean velocity can be expressed as $U_\infty - U(x, r) = u_0(x)f(x, \eta)$, where U_∞ is the free stream velocity, $u_0 = U_\infty - U(x, r = 0)$ is the mean velocity deficit along the centerline, and $\eta(x) = r/\delta(x)$ is a nondimensional scale normalized by a characteristic wake width $\delta(x)$ with $\delta^2(x) = \frac{1}{u_0}\int_0^\infty (U_\infty - U)r\,\mathrm{d}r$. If $f(x, \eta)$ is independent of x and a function only of η, $f(x, \eta)$

*Corresponding author: yizhou@njust.edu.cn

could be simplified to $f(\eta)$, then the mean streamwise velocity is self-similar. A more detailed definition of the self-similarity behavior of a quantity can be found in the textbook by Pope [2]. It is well-known that it can be faster for a low-order variable (e.g., mean velocity) to become self-similar when compared with high-order/complex variables (e.g., Reynolds shear stress, dissipation rate, and kinetic energy) [1].

Parallel to the statistical theory of free shear flows, another line of enquiry, concerns the so-called coherent/vortex structures in the instantaneous turbulent flow field. The study on coherent structures goes back to Helmholtz [3], who proposed the concept of vortex tube/filament. Küchemann [4] described the vortex motions as "the sinews and muscles of fluid motions". She *et al.* [5] presented the early numerical evidence for the existence of the long-lived tubelike structures, which is closely related to the spatial intermittecy, by means of direct numerical simulation (DNS). Hussain [6] viewed the coherent structures as a connected, large-scale turbulent fluid mass with phase-correlated vorticity over its spatial extent. We now know that there are multiscale vortex structures in various kinds of turbulence (i.e., the small-scale streamwise vortex structures and the very large–scale vortex structures), which are more formally called coherent structures [7].

Over the past three decades, various vortex identification criteria [8] have been proposed, including Q (i.e., the second invariant of velocity gradient tensor) [9], λ_2 (i.e., a pressure Hessian criterion) [10], and λ_{ci} (i.e., the imaginary part of complex conjugate eigenvalue) criterion [11]. These methods (e.g., Q, λ_2, λ_{ci}) are generally based on Cauchy-Stokes decomposition and the velocity gradient tensor eigenvalue, and can be used for some qualitative understanding of turbulence. The coherent structures can be visualized by the isosurface of vorticity or other methods, but all these methods mentioned rely on a subjective selection of the identification threshold [8].

Based on the research of Li *et al.* [12], Liu *et al.* [13], and Wang *et al.* [14] recently proposed the so-called Liutex method, which provides strict mathematical definitions of the local rigid rotation of a fluid point (e.g., rotational vector, the local rotation axis, and also rotation strength). Gao *et al.* [15] further used the Liutex method and the intersection point of Liutex magnitude gradient line to identify the vortex core center and the vortex axis. The Liutex method allows us to quantitatively study the spatial distribution and also the organization of the coherent structures.

Quite recently, axisymmetric turbulent wake behind a bluff plate with irregular/fractal edges has been studied numerically [16–18] and experimentally [16–19]. Nedić *et al.* [19] reported a nonequilibrium similarity scaling law concerning energy dissipation in an axisymmetric turbulent wake. Employing an assumption of constant anisotropy and the nonequilibrium energy dissipation law, Dairay *et al.* [16] derived a universal scaling of the wake-width and the velocity deficit. Zhou and Vassilicos [17] have proved that in an axisymmetric turbulent wake the probability density function (PDF) of the radial positions of the turbulent/nonturbulent (T/NT) interface at different downstream locations is self-similar and further investigated the energy transfer near the T/NT interface [18]. They found that the interscale energy transfer near the T/NT interface is mainly from small scale to large scale in the direction near the tangent plane of the interface, suggesting that fluid motions are mostly stretching.

As a continuation of the previous studies [17,18], the main purpose of this paper is to study the spatial distribution of coherent structures in a self-similar axisymmetric turbulent wake by resorting to the vortex identification method proposed by Liu *et al.* [13]. The coherent structures provide a possible means to connect between scales in multiscale physical processes (see for instance, Motoori and Goto [20]), and the spatial distribution of the vortex core center and the origination of vortex axis are important physical features of the coherent structures. It is worth mentioning that the turbulence statistics in the axisymmetric wake acquire the self-similar behavior within a limited downstream range [16], which enables us to numerically explore the characteristics of coherent structures in the self-similar region of a spatially developing wake. The organization of this paper is as follows. In Sec. II, we briefly introduce the simulation conditions and numerical methods. In Sec. III, the T/NT interface and the vorticity field are visualized. The coherent structures are visualized by the Omega method [21] and the vortex core center and vortex axis are identified by the Liutex method [22]. The statistics of the positions of the vortex core center, the direction of the vortex axis, and

TABLE I. Geometry details and numerical parameters.

Re_{in}	X_p/L_b	L_x/L_b	L_y/L_b	L_z/L_b	N_x	N_y	N_z
5000	10	120	15	15	3841	480	480

the radial distance between the interface and the nearest vortex core center are calculated and the corresponding scaling laws are obtained. Finally, the main conclusions are given in Sec. IV.

II. NUMERICAL DETAILS

In this work, DNS is performed to investigate the spatial distribution of coherent structures in a spatially developing axisymmetric turbulent wake. Table I shows the geometric details and numerical parameters. The geometry details of the mimicked bluff fractal plate (e.g., the fractal dimension $D_f = 1.5$ and the surface area A) and numerical parameters are exactly the same as those developed by Dairay *et al.* [16] and Zhou and Vassilicos [17]. The inlet Reynolds number determined by the inlet mean velocity U_∞ is $Re_{in} = U_\infty L_b/\nu = 5000$, where ν is the (constant) kinematic viscosity and the reference length L_b is defined as $L_b = \sqrt{A}$. The Cartesian coordinate system $(O; x, y, z)$ is adopted for the numerical simulation. The coordinates x, y, and z represent the streamwise, vertical, and spanwise directions, respectively. The X_p is the streamwise distance from the inlet to the bluff plate, which is placed normal to the incoming laminar free stream, and the origin of the coordinate system O is placed at the center point of the bluff plate. The lengths L_x, L_y, and L_z represent the dimensions of the computational domain in the x, y, and z directions, respectively. The size of the computational domain is $L_x \times L_y \times L_z = 120L_b \times 15L_b \times 15L_b$ with the corresponding mesh grids of $N_x \times N_y \times N_z = 3841 \times 480 \times 480$.

The incompressible Navier-Stokes equations are solved using the high-fidelity massive-parallel code Incompact3d [23,24], which is based on the sixth-order compact schemes for spatial discretization on a Cartesian mesh and a third-order Adams-Bashforth scheme for time advancement. The collection of turbulent statistics is obtained over a time of $T = 4000L_b/U_\infty$ corresponding to approximately 436 vortex shedding periods. One can find further descriptions and the validation of the DNS of the axisymmetric turbulent wake in Dairay *et al.* [16] and Zhou and Vassilicos [17].

III. RESULTS AND DISCUSSION

A. Flow Visualization

Before delving into the spatial distribution of coherent structures in the self-similar axisymmetric turbulent wake, the visualization of the coherent structures and the method used to identify the vortex core center and the vortex axis are given.

In previous studies [25–27], the magnitude of vorticity $|\boldsymbol{\omega}|$ (i.e., $\boldsymbol{\omega}$ represents the vorticity vector) is used to detect the T/NT interface. It should also be mentioned that throughout this paper, the bold letters represent vectors and the operator "| |" represents the magnitude of a vector. The magnitude of vorticity $|\boldsymbol{\omega}|$ is defined as $|\boldsymbol{\omega}| = (\omega_i\omega_i)^{1/2}$ with $\omega_i = \varepsilon_{ijk}\partial u_k/\partial x_j$ [28]. For the instantaneous velocity components u_i, the indices $i = 1$, 2, and 3 denote the instantaneous velocity components in the x, y, and z directions, respectively. Similarly, the notations x_1, x_2, and x_3 represent the x, y, and z directions, respectively.

Following Zhou and Vassilicos [17], we also use the vorticity threshold $|\boldsymbol{\omega}|_{th}/|\boldsymbol{\omega}|_{max} = 4 \times 10^{-4}$ to identify the outer edge of the T/NT interface with $|\boldsymbol{\omega}|_{max}$ being the instantaneous maximum magnitude of vorticity on a streamwise cross section. Figures 1(a) and 1(b) show randomly selected snapshots of the vorticity field and the outer edge of the T/NT interface at $x/L_b = 50$ and 80 at the same time, respectively. The outer edge of the T/NT interface is represented by the white solid line, which separates the turbulent region and the non-turbulent region. At both locations, the outer

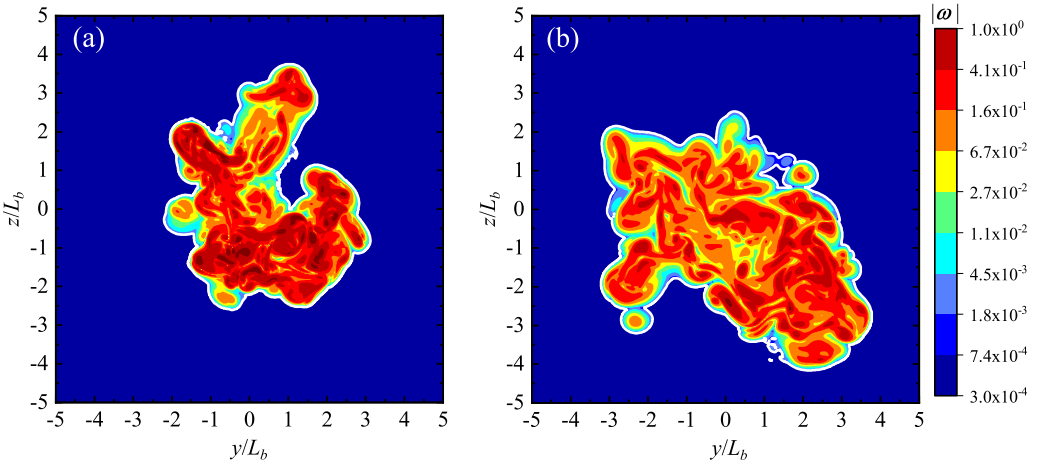

FIG. 1. Visualization of the vorticity field and the T/NT interface in the y-z plane at (a) $x/L_b = 50$ and (b) $x/L_b = 80$ at a same time, i.e., $T = 1000U_\infty/L_b$.

edge of the T/NT interface has a convoluted shape. It can been seen that in the turbulent region starting from the outer edge of the interface the magnitude of vorticity $|\boldsymbol{\omega}|$ increases rapidly as that has already been extensively reported in previous studies [25–27]. Owing to the existence of intermittent structures, even in the deep turbulent region far away from the interface the magnitude of vorticity $|\boldsymbol{\omega}|$ is not uniformly distributed.

To identify the coherent structures, throughout this paper, the isosurface of a scalar variable Ω proposed by Liu *et al.* [22] is visualized. Note that the scalar variable Ω is not a part of the Liutex method. The variable Ω can be expressed as $\Omega = (\frac{1}{2}\omega_i\omega_i)/(\frac{1}{2}\omega_i\omega_i + s_{ij}s_{ij} + m)$, where $s_{ij} = \frac{1}{2}(\partial u_i/\partial x_j + \partial u_j/\partial x_i)$ denotes the symmetric part of the velocity gradient tensor. This scalar variable reflects the ratio of the square of the vorticity to the sum of the squares of the vorticity and the deformation. The correction parameter $m = 0.001 \times (\frac{1}{2}\omega_i\omega_i - s_{ij}s_{ij})_{max}$ is used to avoid the influence of nonphysical noise on the identification of the vortex structure [29]. Following previous studies [21,22,29], the threshold $\Omega = 0.52$ is adopted for the identification of the coherent structures. The reason for using the threshold $\Omega = 0.52$ is that it has been argued to be rather robust and applicable to a variety of turbulent flows [21,22,29].

Figures 2(a) and 2(b) show the coherent structures visualized by the isosurface of $\Omega = 0.52$ and by the threshold with $|\boldsymbol{\omega}| = 0.4U_\infty/L_b$ in the streamwise range $50 \leqslant x/L_b \leqslant 100$ at the same time as Fig. 1, respectively. In Figs. 2(a) and 2(b), we observe remarkably similar contours of the three-dimensional coherent structures. The spatial distribution of coherent structures are periodical. Obviously, the periodical pattern is caused by the large-scale vortex shedding behavior. The spiral tubelike structures shown in Fig. 2 are highly intermittent and not uniformly distributed. It can be also seen that the coherent structures swirl around the centerline with downstream distance.

The spatial distribution of the vortex core center and the organization of the vortex axes are important physical characteristics of the coherent structures. We adopt to the Liutex method mentioned in the introduction section to quantitatively study the spatial distribution of the coherent structures. The Liutex method is based on the idea that albeit the vorticity is always related to the fluid rotation, it cannot correctly (or accurately) describe the local fluid rotation at a given spatial point. Liu *et al.* [22] further argued that the vorticity vector $\boldsymbol{\omega}$ can be decomposed into two parts: the rotational vector (also known as Liutex vector) $\boldsymbol{R}$ and the nonrotational vector $\boldsymbol{S}$ (shear and/or deformation of a fluid element). The rotational vector $\boldsymbol{R} = |\boldsymbol{R}|\boldsymbol{r} = \{\langle\boldsymbol{\omega}, \boldsymbol{r}\rangle - \sqrt{\langle\boldsymbol{\omega}, \boldsymbol{r}\rangle^2 - 4\lambda_{ci}^2}\}\boldsymbol{r}$, where $\langle\boldsymbol{\omega}, \boldsymbol{r}\rangle$ is the magnitude of vorticity in the direction of $\boldsymbol{r}$ with $\boldsymbol{r} = [r_1, r_2, r_3]^T$ being a unit vector parallel to the

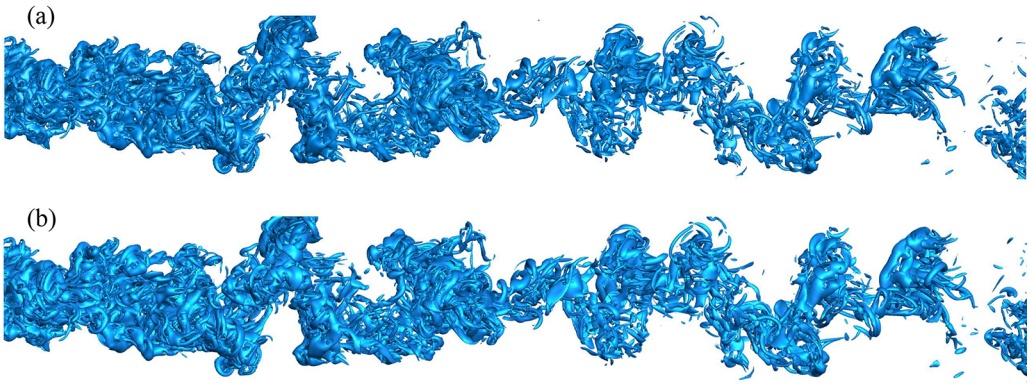

FIG. 2. Instantaneous visualization of the coherent structures in the range of $50 \leqslant x/L_b \leqslant 100$. Isosurfaces with (a) $\Omega = 0.52$ and (b) $|\boldsymbol{\omega}| = 0.4U_\infty/L_b$.

rotational vector $\boldsymbol{R}$ and λ_{ci} being the imaginary part of complex conjugate eigenvalue of the velocity gradient tensor [21]. The detailed formula of computing $\boldsymbol{r}$ can be found in the Appendix and also Liu *et al.* [13] [see Eq. (29) therein]. The nonrotational vector $\boldsymbol{S}$ is as follows:

$$\boldsymbol{S} = \boldsymbol{\omega} - \boldsymbol{R}. \tag{1}$$

The correlation between the vorticity vector $\boldsymbol{\omega}$, the rotational vector $\boldsymbol{R}$, and the non-rotational vector $\boldsymbol{S}$ can be expressed as follows:

$$|\boldsymbol{\omega}|^2 = |\boldsymbol{R}|^2 + |\boldsymbol{S}|^2 + 2|\boldsymbol{R}||\boldsymbol{S}|\cos\theta, \tag{2}$$

where θ is the angle between $\boldsymbol{R}$ and $\boldsymbol{S}$. Note that the magnitudes of $\boldsymbol{R}$ and $\boldsymbol{S}$ (i.e., $|\boldsymbol{R}|$ and $|\boldsymbol{S}|$) represent the local rotational strength and nonrotational strength of fluid motions, respectively.

The vortex core center is mathematically defined as a fluid point where the cross product of $\nabla|\boldsymbol{R}|$ and $\boldsymbol{R}$ equals zero, that is, $\nabla|\boldsymbol{R}| \times \boldsymbol{r} = 0$ [15]. The vortex axis is a line that aligns the Liutex magnitude gradient vector $\nabla|\boldsymbol{R}|$ and the rotational vector $\boldsymbol{R}$, where $\nabla|\boldsymbol{R}| = (\partial|\boldsymbol{R}|/\partial x, \partial|\boldsymbol{R}|/\partial y, \partial|\boldsymbol{R}|/\partial z)$ [15]. The vortex axis can be computed by integrating $\boldsymbol{R}$ passing through the vortex core center. For further information concerning the identification of the vortex core center and vortex axis, one could refer to previous relevant studies (see, for example, Liu *et al.* [22], Dong *et al.* [29], and Wang *et al.* [30]).

Figures 3(a) and 3(b) show the snapshots of the magnitude of Liutex field $|\boldsymbol{R}|$, the outer edge of the T/NT interface, and the vortex core center in the y-z plane at two different streamwise locations $x/L_b = 50$ and 80, respectively, which is taken at the same time $T = 1000U_\infty/L_b$ as Fig. 1. The solid black points shown in Fig. 3 represent the vortex core centers, which are given by $\nabla|\boldsymbol{R}| \times \boldsymbol{r} = 0$. The vortex core center is sparsely distributed within the interface and is surrounded by the strong rotational region. From Eq. (2), it is obvious that the square of the magnitude of vorticity $|\boldsymbol{\omega}|^2$ contains three parts: $|\boldsymbol{R}|^2$, $|\boldsymbol{S}|^2$, and $2|\boldsymbol{R}||\boldsymbol{S}|\cos\theta$. In the turbulent region, there is not only the rotational motion with $|\boldsymbol{R}| > 0$ but also the pure shear motion with $|\boldsymbol{R}| = 0$ and $|\boldsymbol{S}| > 0$, and the pure shear motion mainly occurs near the outer edges of the T/NT interface (the white solid lines), as shown in Fig. 1.

Previous numerical studies [31–33] have revealed that the T/NT interface is composed of two different sublayers: viscous superlayer (a thin inner layer close to the outer edge of the T/NT interface) and turbulent sublayer (a layer with a sharp increase in the vorticity but slightly away from the T/NT interface). In the viscous superlayer, viscous diffusion effects are dominant in the increase of the vorticity magnitude, whereas in the turbulent sublayer the inviscid vortex stretching becomes significant [34,35]. Figures 3(a) and 3(b) clearly suggest that in the viscous superlayer close to the outer edge of the T/NT interface, we have $|\boldsymbol{\omega}|^2 = |\boldsymbol{S}|^2$, implying that the influence

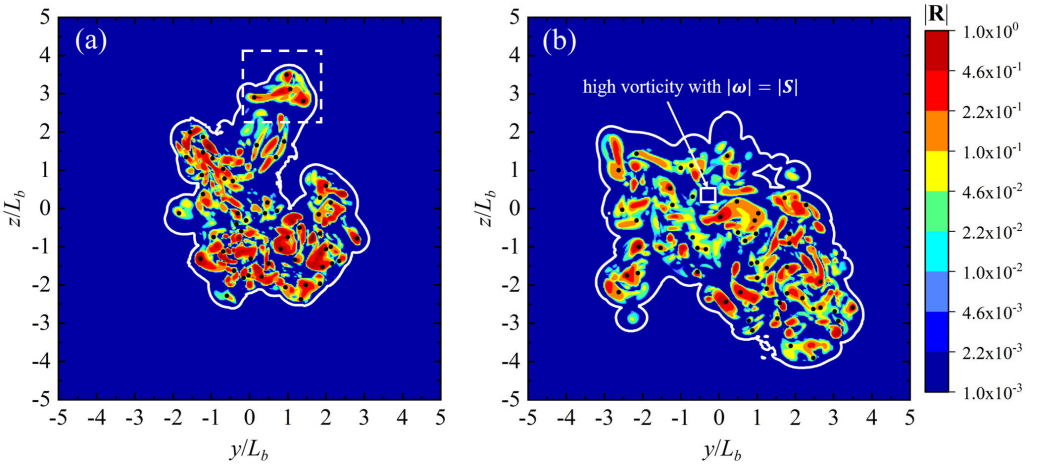

FIG. 3. Visualization of the magnitude of Liutex field, the outer edge of the T/NT interface, and the vortex core center at two different streamwise locations; (a) $x/L_b = 50$ and (b) $x/L_b = 80$. In (b), the boxed area presents the high vorticity region with $|\boldsymbol{\omega}| = |\boldsymbol{S}|$.

of the pure shear motions is dominant. When comparing Fig. 1(a) and Fig. 3(a) [or equivalently Fig. 1(b) and Fig. 3(b)], another interesting finding is that even though in the turbulent core regions where the magnitude of the vorticity is high, there exist some regions with the same characteristics as the viscous superlayer (e.g., the boxed region in Fig. 3(b)].

Figures 4(a) and 4(b) show an enlargement of the content of the white dashed box in Fig. 3(a) (i.e., two-dimensional distribution of the magnitude of the Liutex field) and also the isosurface of the three-dimensional coherent structure of $\Omega = 0.52$ along with the corresponding internal rotation axis, respectively. It should also be mentioned that the vortex core region A in Fig. 4(a) represents the same high Liutex region as indicated by region A in Fig. 4(b) (the same case for region B). The streamline (the black solid line) in the partial y-z plane at $x/L_b = 50$ is also included in Fig. 4(a). It is suggested that the streamline forms a vortex pattern with its center being designated as the vortex

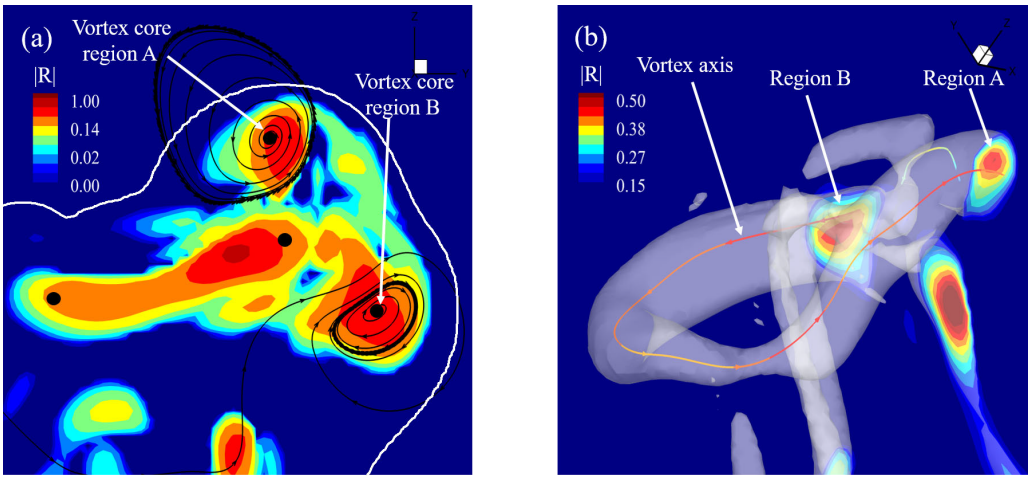

FIG. 4. (a) Instantaneous magnitude of Liutex field $|\boldsymbol{R}|$ and (b) the coherent structures and the internal rotation axis at the streamwise location of $x/L_b = 50$.

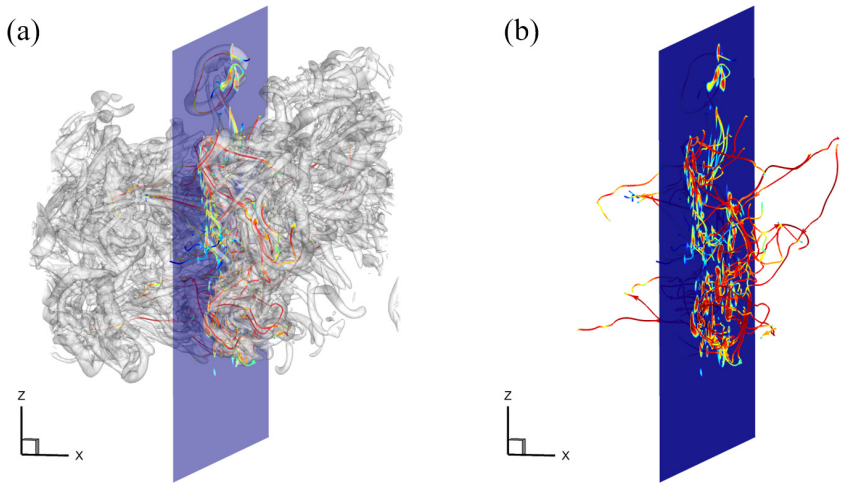

FIG. 5. (a) Coherent structures within the streamwise range $47.5x/L_b \leqslant 52.5$ and (b) the corresponding vortex axes on the transparent section of $x/L_b = 50$ at the same time shot as Figs. 3 and 4.

core center [36]. The center of the two chosen streamlines can be superposed with the vortex core center, which proves that the vortex core center can be indeed accurately identified. As shown in Fig. 4(b), the transparent white part with $\Omega = 0.52$ represents the coherent structures, and the color of the internal rotation axis represents the rotational strength $|\boldsymbol{R}|$, where the internal rotation axis is also known as the vortex axis. One may draw the conclusion that the internal rotation axis can reflect the general contour of the corresponding coherent structure, at least to some extent.

Figure 5(a) shows the distribution of coherent structures (represented by the white isosurface with $\Omega = 0.52$) in the three-dimensional subdomain within the streamwise range $47.5 \leqslant x/L_b \leqslant 52.5$ at the same time shot as Figs. 3 and 4. In Fig. 5(b), the corresponding vortex axes with $\nabla|\boldsymbol{R}| \times \boldsymbol{r} = 0$ and $|\boldsymbol{R}| > 0$, which intersect the lateral plane at $x/L_b = 5$ are plotted. There are a considerable number of intermittently distributed spiral coherent structures along with the corresponding vortex axes, which enables us to quantitatively study the organization and also spatial distribution of the coherent structures and will be discussed in detail below.

B. Spatial distribution and the organization of coherent structures

Following the study of Zhou and Vassilicos [17], we concentrate attention in the region of $50 \leqslant x/L_b \leqslant 100$ where the time-averaged area of turbulent region scales with δ^2 and the PDF of the radial locations of the T/NT interface is self-similar. Note that previous studies [16,17] have confirmed that the profiles of the one-point turbulence statistics (e.g., the streamwise mean velocity, Reynolds shear stress, turbulent kinetic energy, and turbulent dissipation) and the PDF of radial interface location R_I in the axisymmetric turbulent wake are self-similar in the range of $10 \leqslant x/L_b \leqslant 100$, that is the so-called self-similar region. In the following subsection, the spatial distribution of coherent structures in the self-similar region is discussed. Considering the fact that the choice of the threshold for the identification of the coherent structures can be somewhat arbitrary, the radial positions of the vortex core center R_c of the coherent structures at different streamwise locations are computed. For a given vortex center in the y-z at the streamwise location x, the corresponding radial distance R_c is defined as the radius distance locations of the vortex core center away from the centerline. In order to compute the conditional statistics of the organization of the coherent structures, we define a new local coordinate system, in which the origin is exactly the vortex core center and the selection of the three coordinates is the same as the old coordinate system, i.e., x, y, and z. Based on the new local coordinate system, the organization of the coherent

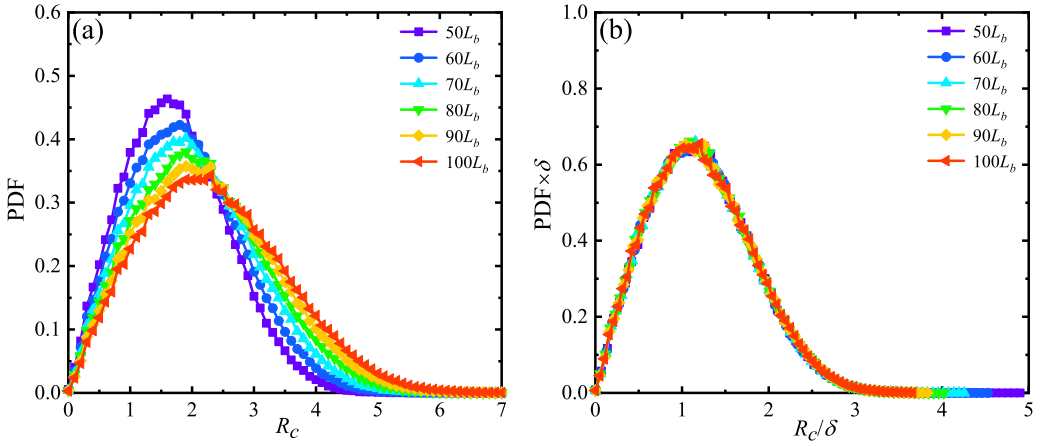

FIG. 6. PDFs of the radial positions of the vortex core center; (a) $P(R_c;x)$ versus R_c at different streamwise locations and (b) $\delta(x)P(R_c;x)$ versus $R_c/\delta(x)$ at different streamwise locations.

structures [i.e., the polar angle α and the azimuthal angle φ of the vortex axes with $\alpha \in [0, \pi]$ and $\varphi \in [0, 2\pi)$] at different streamwise locations can be explored. The polar angle α is the angle between the streamwise direction and the vortex axis and the azimuthal angle φ of the vortex axis is in the y-z plane normal to the wake centerline. It should also be mentioned that the vortex axis in Fig. 4(b) can be also extracted by connecting the vortex core center in a given coherent structure.

Figure 6 shows the PDFs of the radial distribution of the vortex core center R_c in the range of $50 \leqslant x/L_b \leqslant 100$, where one of $P(R_c;x)$ versus R_c at different streamwise locations and one of $\delta(x)P(R_c;x)$ versus $R_c/\delta(x)$ at different streamwise locations. The radial locations of the vortex core center R_c are obtained from the intersections of the vortex core center with radial straight lines at various azimuthal angles γ in the y-z plane at x. As shown in Fig. 6(a), the profiles of the PDFs of R_c are quite different from each other. In contrast, Fig. 6(b) shows that the PDFs of R_c at different streamwise locations can be superimposed on the same curve when normalized by the wake width δ, which indicates that the PDF $P(R_c;x)$ takes a self-similar form. In other words, with the different streamwise locations, the PDFs of R_c scale with δ. The probabilities of R_c at different streamwise locations reach the maximum value at $R_c \approx 1.16\delta$. The exceedance probability of R_c by $R_c = 3\delta$ drops to less than 0.007, as calculated by integrating the distribution function from 3δ to positive infinity and nearly all of the vortex core centers are located within this separation distance. Figure 6(b) further reveals that the coherent structures are not randomly distributed in the self-similar region, and this is closely related to the wake width δ. It has been investigated that the averaged interfacial radius $\overline{R_I}(x)$ (the overbar denotes an average over the azimuthal angle γ and time T) in the lateral y-z plane normal to the streamwise direction proposed by Zhou and Vassilicos [17] is a function of x [i.e., $\overline{R_I}(x) \approx 1.6\delta(x)$]. The radial interface locations R_I are obtained from the intersections of the interface with radial straight lines at various azimuthal angles γ in the y-z plane at x. The averaged radial distance $\overline{R_c}(x)$ of the vortex core center satisfies the following relation:

$$\overline{R_c}(x) \approx 1.22\delta(x). \tag{3}$$

The scaling $\overline{R_c}(x) \approx 1.22\delta(x)$ suggests that there is an intrinsic connection between the mean streamwise velocity and the spatial distribution of the coherent structures.

Another interesting finding related to the radial distribution of the core center is that the probability distributions are generally in accord with the Reynolds shear stress profiles $\langle u_x u_r \rangle$ and for both distributions the maximum values are found at the radial position with $R/\delta \approx 1.1$ (see Fig. 18 in Dairay *et al.* [16]). It should also be mentioned that the main purpose of this work is to study the spatial distribution of the coherent structures. The intrinsic correlation between the distributions

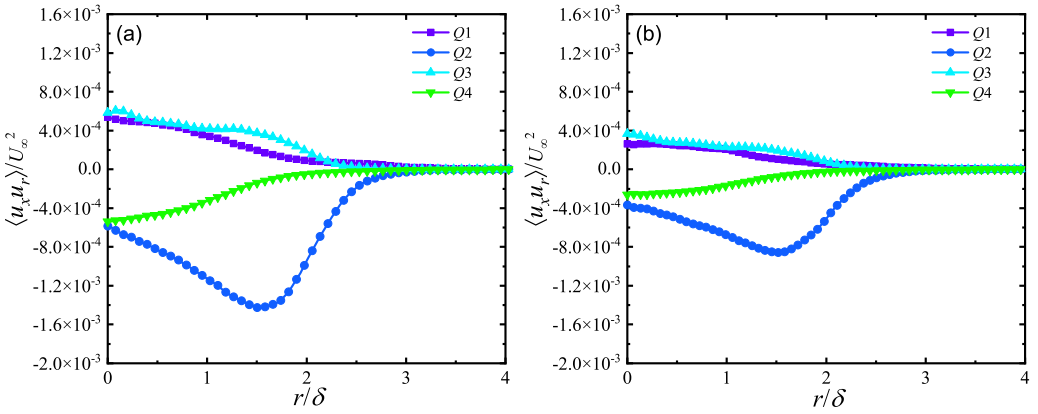

FIG. 7. Contributions of the four quadrants to the Reynolds shear stress $\langle u_x u_r \rangle$ at two downstream locations (a) $x/L_b = 60$ and (b) $x/L_b = 90$.

of the coherent structures and the one-point statistics in free shear flows can also be of significant importance.

The generation of Reynolds shear stress in wall-bounded flows, such as channel flow and turbulent boundary layers, has been extensively studied through quadrant analysis [37]. It has long been known that the contributions of the ejection and sweep events (i.e., Q2 events and Q4 events) to Reynolds shear stress are dominant in a turbulent boundary layer and both Q2 and Q4 events are closely related to the coherent structures [38–40]. In an axisymmetric turbulent wake, the Reynolds shear stress, that is the product of the streamwise and the radial velocity fluctuations u_x and u_r, can also be divided into four categories: Q1 ($u_x > 0, u_r > 0$), Q2 ($u_x < 0, u_r > 0$), Q3 ($u_x < 0, u_r < 0$), and Q4 ($u_x > 0, u_r < 0$) with Q2 and Q4 corresponding to the ejection and sweep events, respectively [37,41,42]. Figures 7(a) and 7(b) depict the conditional averages of the Reynolds shear stress for the four quadrants, representing the contributions to the Reynolds shear stress at two different downstream locations: $x/L_b = 60$ and 90, respectively. The magnitudes of the conditional Reynolds stress corresponding to Q1, Q3, and Q4 quadrants are comparable. In contrast, the contribution of Q2 (i.e., ejection events) is significantly large, suggesting the dominance of outward momentum transport. It should also be mentioned that this observation does not necessarily contradict the case of turbulent boundary layers. For the turbulent boundary layers only in the near wall region is the influence of Q4 significantly larger than Q2, and as the distance from the wall increases, the reverse occurs [37,41].

Figure 8 shows the contributions of the four quadrants to the Reynolds shear stress conditioned on being part of a coherent structure with $|\boldsymbol{\omega}| \geqslant 0.4U_\infty/L_b$, i.e., $\langle u_x u_r || \boldsymbol{\omega}| \geqslant 0.4U_\infty/L_b \rangle$. The conditional averaged results are fluctuating for the limited sample data at the downstream location $x/L_b = 90$. It is assumed that the conditional average magnitude is zero for the quadrant where no fluid points with $|\boldsymbol{\omega}| \geqslant 0.4U_\infty/L_b$. A preference for Q2 events is also evident, as shown in figure 7, and the conditional strength of Q2 is comparable to the unconditional magnitude. Therefore, the coherent structures are not quiescent patches but are indeed related to Q2 events.

Another significant finding is that the profiles of the conditional Reynolds stress are similar to each other for both streamwise locations $x/L_b = 60$ and 90. Additionally, the most intense ejection events are observed at approximately 1.5δ. This location is slightly different from the averaged radial distance of the vortex core center $\overline{R_c}(x) \approx 1.22\delta(x)$. One possible explanation is that in this work coherent structures are identified based on the instantaneous velocity fields, while the Reynolds shear stress is directly determined by the velocity fluctuations and influenced by the mean velocity gradients. It should also be mentioned that although only the conditional averages of the Reynolds stress at two locations are plotted for the sake of space economy, we confirm that

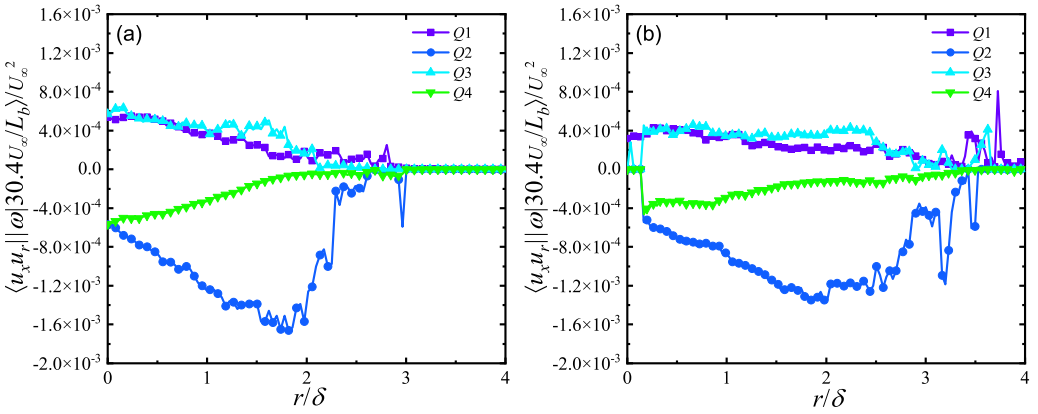

FIG. 8. The same as Fig. 7 but conditioned on being part of a coherent structure with $|\boldsymbol{\omega}| \geqslant 0.4U_\infty/L_b$.

the scaling $R_{Q4,max}(x) \approx 1.5\delta(x)$ can be applied to other downstream locations within the range of $50 \leqslant x/L_b \leqslant 100$. The above discussion lends credence to the existence of a close relationship between the distributions of the coherent structures and the one-point statistics.

Figures 9(a) and 9(b) show the PDFs of the polar angle α and the azimuthal angle φ of the vortex axis in the range of $50 \leqslant x/L_b \leqslant 100$, respectively. It can be seen that the PDFs of the polar angle α between the vortex axis and the streamwise direction at different streamwise locations collapse onto a single curve, which indicates that the PDF $P(\alpha; x)$ takes a self-similar form. The probabilities of α at different streamwise locations reach the maximum value at $\alpha = \pi/2$, implying a noticeable preference for the vortex axis (or equivalently coherent structures) to be normal to the mean direction of the flow. As shown in Fig. 5, the visualized spiral structures show a discernible tendency to be parallel to the y-z plane (or equivalently perpendicular to the mean direction of the flow). This observation is consistent with PDF distribution of the polar angle α [see Fig. 9(a)]. The azimuthal angle φ in the lateral y-z plane is uniformly distributed in the range $[0, 2\pi)$ since all the curves in Fig. 9(b) can be superimposed on a single horizontal straight line as it should be.

Figures 10(a) and 10(b) plot the joint PDFs of the polar and azimuthal angles, i.e., α and φ at $x/L_b = 50$ and 80, respectively. Figure 10 suggests that at both streamwise locations considered for

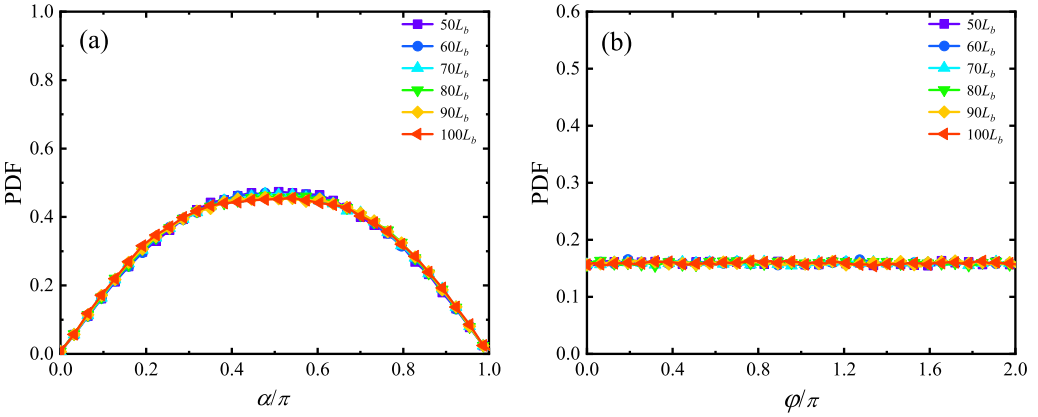

FIG. 9. PDFs of the polar angle α and the azimuthal angle φ about the vortex axis; (a) $P(\alpha; x)$ versus α at different streamwise locations and (b) $P(\varphi; x)$ versus φ at different streamwise locations.

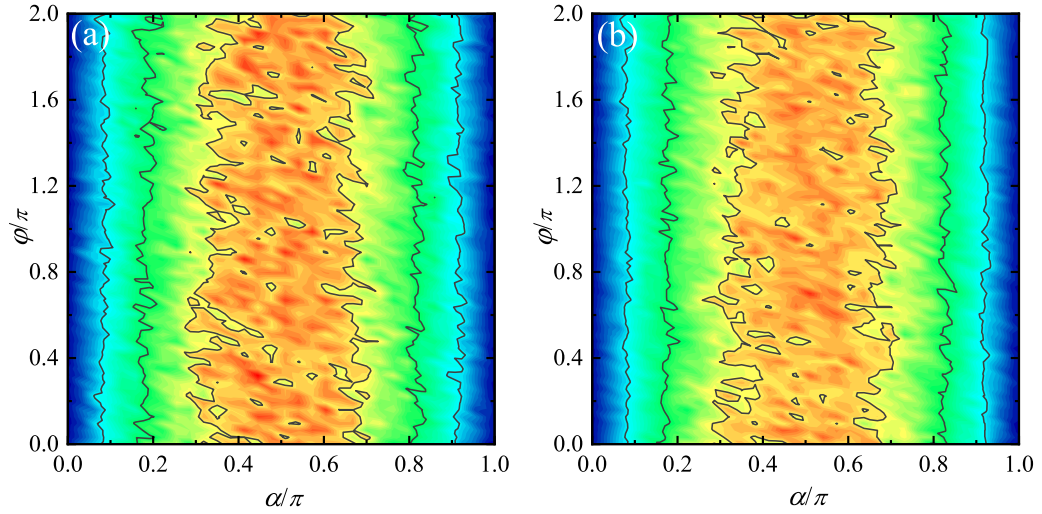

FIG. 10. Joint PDFs of α and φ at two different downstream locations; (a) $x/L_b = 50$, (b) $x/L_b = 80$, the four contour levels plotted are 3×10^{-2}, 5×10^{-2}, 7×10^{-2}, and 9×10^{-2}, respectively.

a given polar angle α, the probability distribution of the azimuthal angle φ is approximately uniform, and vice versa. The correlation $\rho(\alpha, \varphi)$ equals to 0.5% and 0.2% at $x/L_b = 50$ and 80, respectively, implying that there is no statistical correlation between the polar angle α and the azimuthal angle φ. Comparing Figs. 9 and 8, it can be concluded that the coherent structures are regularly organized in space, i.e., the PDF $P(\alpha; x)$ and $P(\varphi; x)$ take the self-similar form and with no discernible correlation between α and φ.

C. Coherent structures near the turbulent/non-turbulent interface

Previous numerical studies by da Silva and Taveira [43] and da Silva and dos Reis [44] have already found that the radial size of the coherent structures define the contorted shape of the nearby interface, and the coherent structures can influence the viscous dissipation of kinetic energy near the outer edge of the T/NT interface, which clarifies a close relationship between the coherent structures and the T/NT interface. In this section, we shall explore the mean radial distance between the T/NT interface and the coherent structures nearby.

Figure 11(a) shows the three-dimensional visualization of the T/NT interface and the coherent structures in the range of $47.5 \leqslant x/L_b \leqslant 52.5$ from a different time shot as in Fig. 1. The translucent blue represents the T/NT interface, and the coherent structures are visualized by the isosurface (white) of $\Omega = 0.52$. The T/NT interface is convoluted and envelops the coherent structures, and the T/NT interface is close to the exterior surface of the coherent structures. Figure 11(b) shows the snapshot of the magnitude of Liutex field $|\boldsymbol{R}|$, the outer edge of the T/NT interface and the vortex core center in the selected translucent dark blue in the y-z plane in Fig. 11(a). It has been reported that the PDF of the radial interface location [17] and the PDF of the radial distribution of the vortex core center are self-similar in the range of $50 \leqslant x/L_b \leqslant 100$. The intrinsic correlation between the T/NT interface and the vortex core center can be further analyzed by the radial separation distance R_{ct} between the T/NT interface and the nearest vortex core center at different azimuthal angles γ [see Fig. 11(c) on the calculation of R_{ct}]. For a given azimuthal angle γ we have $R_{ct} = R_I - R_c$. It is worth mentioning that there are other different definitions of the thickness of the T/NT interface (e.g., distance between the outer edge of the T/NT interface and the maximum conditional mean vorticity [43,44] and the derivative of the conditional mean vorticity [45,46]). Furthermore, previous investigations [43–46] on the conditional statistics of the thickness are based on the contour of the

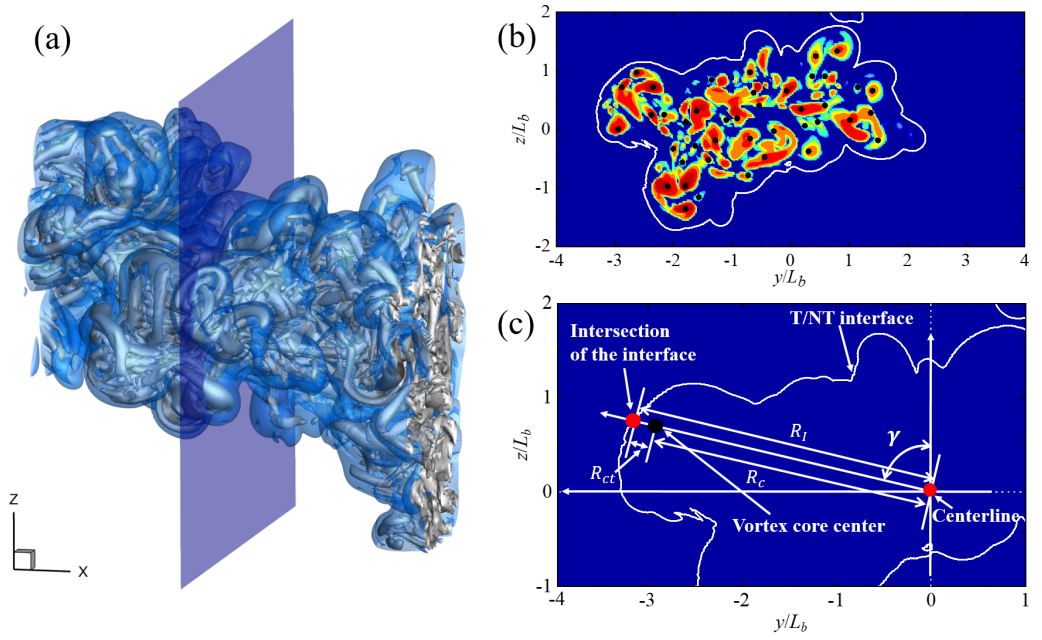

FIG. 11. (a) Three-dimensional visualization of the T/NT interface and coherent structures in the range of $47.5 \leqslant x/L_b \leqslant 52.5$ ($|\boldsymbol{\omega}|_{th}/|\boldsymbol{\omega}|_{max} = 4 \times 10^{-4}$), (b) visualization of the magnitude of Liutex field, the outer edge of the T/NT interface, and the distribution of the vortex core center, and (c) the schematic diagram on the calculation of R_{ct}.

T/NT interface, whereas in our work a fixed cylindrical coordinate is used to estimate R_{ct} [see Fig. 11(c)].

Figures 12(a) and 12(b) show the PDFs of the distance R_{ct} between the T/NT interface and the nearest vortex core center in the range of $50 \leqslant x/L_b \leqslant 100$, where one of $P(R_{ct}; x)$ versus R_{ct} at different streamwise locations and one of $\delta(x)P(R_{ct}; x)$ versus $R_{ct}/\delta(x)$ at different streamwise locations. Comparing with Fig. 12(a), it can be seen that the PDFs of R_{ct} at different streamwise locations can be superimposed on the same curve when normalized by the wake width δ as shown in Fig. 12(b). In other words, with the different streamwise locations, the PDFs of R_{ct} scale with δ. The probabilities of R_{ct} at different streamwise locations reach their maximum value at $R_{ct} \approx 0.2\delta$ and we have $\overline{R_{ct}}(x) \approx 0.48\delta(x)$. The radial interface location R_I is determined by the radial separation distance R_{ct} and the radial location of the corresponding nearest vortex core center R_c (i.e., $R_I = R_{ct} + R_c$). One could reasonably argue that the PDF distribution of the nearest vortex core center R_c also scales with δ. To some extent, the reasonably good collapse in Fig. 12(b) could explain the finding reported in Zhou and Vassilicos [17] that the PDF of the radial interface location scales with the wake width δ.

Figure 12(c) shows the PDFs of R_{ct} at different streamwise locations normalized by the Taylor microscale λ along the centerline, where $\lambda = \sqrt{15\nu/\varepsilon}\sqrt{2K/3}$ with K being the turbulent kinetic energy and ε being the turbulence dissipation rate. The probabilities of R_{ct} at different streamwise locations reach the maximum value at $R_{ct} \approx 0.8\lambda$. Similar to Fig. 12(b), the normalized profiles of R_{ct} are reasonably well collapsed, and the averaged distance $\overline{R_{ct}}(x)$ satisfies the relation: $\overline{R_{ct}}(x) \approx 2.0\lambda(x)$. The approximate relation $\overline{R_{ct}}(x) \approx 2.0\lambda(x)$ is in accord with the assertion made in da Silva and Taveira [43] that in free shear flows the thickness of the T/NT interface is of the order of the Taylor microscale λ. The non-equilibrium scaling laws $C_\varepsilon \sim (Re_G/Re_l)^m$ with $Re_G = (U_\infty L_b)/\nu$ being the global Reynolds number and $Re_l = (\sqrt{K}\delta)/\nu$ being the local Reynolds number can be used to explain the collapse of the normalized profiles in Fig. 12(c). For the current wake flow

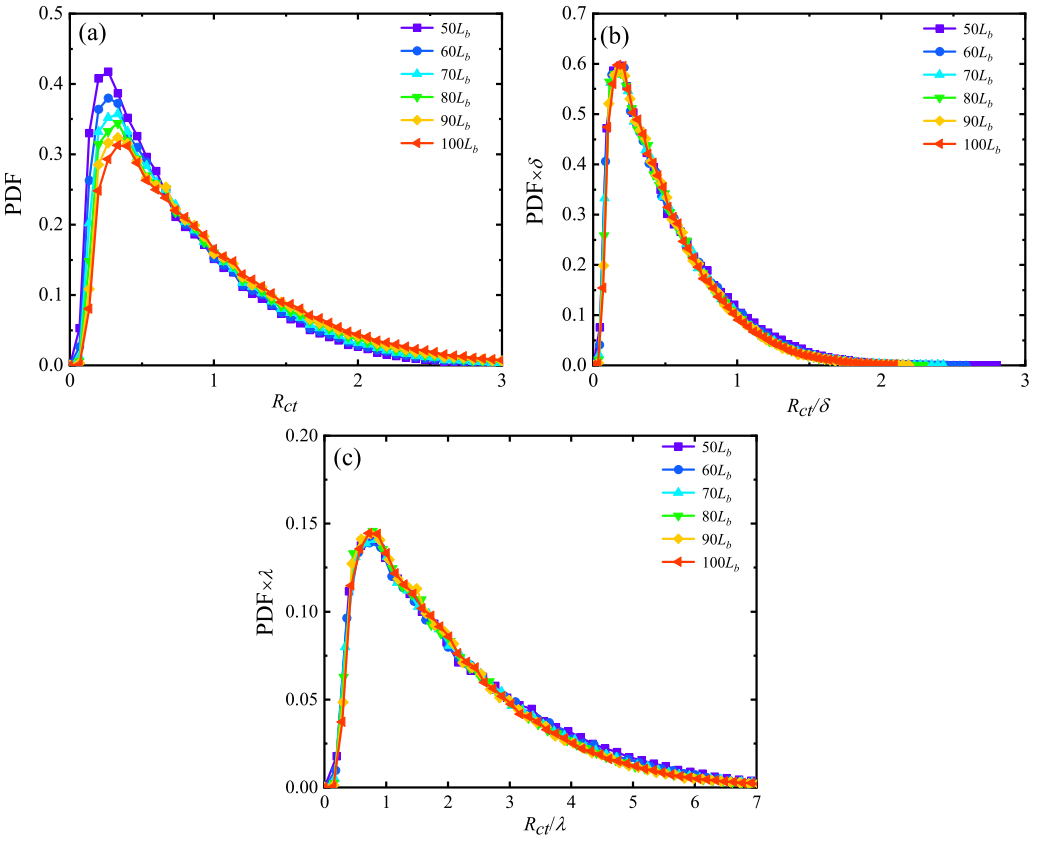

FIG. 12. PDFs of the distance between T/NT interface and nearest vortex core center: (a) $P(R_{ct};x)$ versus R_{ct}, (b) $\delta(x)P(R_{ct};x)$ versus $R_{ct}/\delta(x)$ and (c) $\lambda(x)P(R_{ct};x)$ versus R_{ct}/λ at different streamwise locations.

considered, the local Reynolds number is relatively low and $m = 0.5$ [16]. However, within the downstream range $50 \leqslant x/L_b \leqslant 100$, the value of $C_\varepsilon(Re_l/Re_G)$ varies by no more than 10%, ranging from 0.037 to 0.034 (see Fig. 23(b) in Dairay *et al.* [16]). One could easily derive the scaling law $\lambda \sim \delta$ when $C_\varepsilon(Re_l/Re_G) = const$, which is indeed the case for the turbulent wake with a sufficient high local Reynolds number. Therefore, the fairly satisfactory collapse observed in Fig. 12(c) is reminiscent of the nonequilibrium dissipation law [47,48].

IV. CONCLUSION

The current study can be somewhat regarded as a continuation of the previous investigations [17,18] on turbulence characteristics and the property of T/NT interfaces in an axisymmetric turbulent wake. The main purpose of this work is to shed light on the spatial distribution and organization of the coherent structures in a self-similar axisymmetric turbulent wake.

We firstly explore the spatial distribution and also the organization of the coherent structures (i.e., the direction of the vortex axis). The PDF of the radial distribution of the vortex core center R_c is self-similar and scales with δ, which indicates the spatial distribution of the coherent structures is self-similar. Concerning the organization of the coherent structures, it is concluded that the PDFs of the polar angle α and the azimuthal angle φ at different streamwise locations collapse onto a single curve. There is a significant preference for the coherent structures to be normal to the mean

direction of the flow and no discernible correlation between the polar angle α and the azimuthal angle φ.

The correlation between the T/NT interface and vortex core center and the PDF of the distance R_{ct} between the T/NT interface and the nearest vortex core center are also investigated. The numerical results show that the PDF of R_{ct} is also self-similar and scales with δ. The Gaussian distribution of the radial positions of the T/NT interface reported in Zhou and Vassilicos [17] may be related to the scaling $\overline{R_{ct}}(x) \approx 0.48\delta(x)$.

The current study suggests that for an axisymmetric turbulent wake, there is an intrinsic connection between the self-similar distributions of the one-point statistics and the spatial distribution of the coherent structures. The above observations indeed confirm the assertion by Küchemann [4] that coherent structures are "the sinews and muscles of fluid motions" and further suggest that the coherent structures in a self-similar axisymmetric turbulent wake are orderly distributed and also regularly organized. Future investigations should be performed to check whether this conclusion can be generalized to other free shear flows (e.g., plane jets, plane wakes, mixing layers).

ACKNOWLEDGMENTS

This study was cosupported by the National Natural Science Foundation of China (Grant No. 91952105), the Six Talent Peaks Project in Jiangsu Province (Grant No. 2019-SZCY-005), and the Fundamental Research Funds for Central University (Grant No. 30918011325). Part of this study was also supported by JSPS KAKENHI, Grants No. 22H01398 and No. 22K03937, and JSPS bilateral programs (Grant No. JPJSBP120219916). Part of the numerical simulations were carried out on the supercomputer at Tokoku University (Grant No. J21I016: Institute of Fluid Science, Tohoku University and Grant No. CX33APR21: Advanced Fluid Information Research Center, Institute of Fluid Science, Tohoku University). The author Y.Z. acknowledges the valuable comments from Dr. C. Y. Wang (Nanjing University of Science and Technology).

APPENDIX: DEFINITION OF THE LIUTEX VECTOR $\boldsymbol{R}$

The Liutex-Shear decomposition method, i.e., $\boldsymbol{\omega} = \boldsymbol{R} + \boldsymbol{S}$ is adopted to identify the vortex core center and compute the direction of the vortex axis. The existence of the rotational vector $\boldsymbol{R}$ can be proven using Schur decomposition theory. The procedure for computing the rotational vector $\boldsymbol{R}$ and the corresponding unit vector $\boldsymbol{r}$ is briefly introduced in this Appendix. More detailed explanations can be found in the works of Liu *et al.* [13] and Tian *et al.* [49].

It can be mathematically proven that there exists a transformation matrix $\boldsymbol{Q}$ which projects the velocity gradient tensor $\nabla \boldsymbol{v}$ from the original coordinate system xyz onto $\nabla \boldsymbol{V}$ in a new coordinate system XYZ, which is rotated around the rotational vector $\boldsymbol{r}$ axis, that is, the Z axis is parallel to $\boldsymbol{r}$. We now have

$$\nabla \boldsymbol{v} = \begin{bmatrix} \partial u/\partial x & \partial u/\partial y & \partial u/\partial z \\ \partial v/\partial x & \partial v/\partial y & \partial v/\partial z \\ \partial w/\partial x & \partial w/\partial y & \partial w/\partial z \end{bmatrix}, \tag{A1}$$

$$\nabla \boldsymbol{V} = \begin{bmatrix} \partial U/\partial x & \partial U/\partial y & \partial U/\partial z \\ \partial V/\partial x & \partial V/\partial y & \partial V/\partial z \\ \partial W/\partial x & \partial W/\partial y & \partial W/\partial z \end{bmatrix}, \tag{A2}$$

$$\nabla \boldsymbol{V} = \boldsymbol{Q} \nabla \boldsymbol{v} \boldsymbol{Q}^{-1}. \tag{A3}$$

Using the quaternions method [50] yields

$$\boldsymbol{Q} = \begin{bmatrix} \dfrac{r_y^2 + r_z^2 + r_z}{1 + r_z} & -\dfrac{r_x r_y}{1 + r_z} & -r_x \\ -\dfrac{r_x r_y}{1 + r_z} & \dfrac{r_y^2 + r_z^2 + r_z}{1 + r_z} & -r_y \\ r_x & r_y & r_z \end{bmatrix}, \tag{A4}$$

with $\boldsymbol{r} = r_x \boldsymbol{i} + r_y \boldsymbol{j} + r_z \boldsymbol{k}$.

Owing to the fact that we assume the unit rotational vector $\boldsymbol{r}$ in the original coordinate system is parallel to the Z axis in the new coordinate system XYZ, the Z axis serves as a local rotation axis with $\partial U/\partial Z = 0$ and $\partial V/\partial Z = 0$. By making further use of Eqs. (A1)–(A4), we now get

$$\begin{aligned} \partial U/\partial Z = &\left(1 - \frac{r_x^2}{1 + r_z}\right)\left(\frac{\partial u}{\partial x} r_x + \frac{\partial u}{\partial y} r_y + \frac{\partial u}{\partial z} r_z\right) - \frac{r_x r_y}{1 + r_z}\left(\frac{\partial v}{\partial x} r_x + \frac{\partial v}{\partial y} r_y + \frac{\partial v}{\partial z} r_z\right) \\ &- r_x\left(\frac{\partial w}{\partial x} r_x + \frac{\partial w}{\partial y} r_y + \frac{\partial w}{\partial z} r_z\right) = 0, \end{aligned} \tag{A5}$$

$$\begin{aligned} \partial V/\partial Z = &-\frac{r_x r_y}{1 + r_z}\left(\frac{\partial u}{\partial x} r_x + \frac{\partial u}{\partial y} r_y + \frac{\partial u}{\partial z} r_z\right) + \left(1 - \frac{r_y^2}{1 + r_z}\right)\left(\frac{\partial v}{\partial x} r_x + \frac{\partial v}{\partial y} r_y + \frac{\partial v}{\partial z} r_z\right) \\ &- r_y\left(\frac{\partial w}{\partial x} r_x + \frac{\partial w}{\partial y} r_y + \frac{\partial w}{\partial z} r_z\right) = 0, \end{aligned} \tag{A6}$$

Combining the formula $r_x^2 + r_y^2 + r_z^2 = 1$ and making use of Eqs. (A5) and (A6), we could now compute the unit vector r, the transformation matrix $\boldsymbol{Q}$ and the velocity tensor $\boldsymbol{\nabla V}$.

With respect to the rotation strength, i.e., the magnitude of the rotational vector $|R|$, one needs to use a second coordinate rotation in the X–Y plane, which is normal to the rotation axis. By introducing a rotation matrix, the rotation strength $|R|$ can be expressed in the form of

$$|R| = \begin{cases} 2(\beta - \alpha), & \text{if } \alpha^2 - \beta^2 < 0, \beta > 0 \\ 2(\beta + \alpha), & \text{if } \alpha^2 - \beta^2 < 0, \beta < 0 \\ 0, & \text{if } \alpha^2 - \beta^2 \geqslant 0 \end{cases} \tag{A7}$$

with $\alpha = \frac{1}{2}\sqrt{(\frac{\partial V}{\partial Y} - \frac{\partial U}{\partial X})^2 + (\frac{\partial V}{\partial X} + \frac{\partial U}{\partial Y})^2}$ and $\beta = \frac{1}{2}(\frac{\partial V}{\partial X} - \frac{\partial U}{\partial Y})$.

[1] H. Tennekes and J. L. Lumley, *A First Course in Turbulence* (MIT Press, Cambridge, MA, 1972).

[2] S. B. Pope, *Turbulent Flows* (Cambridge University Press, Cambridge, UK, 2000).

[3] H. Helmholtz, About integrals of hydrodynamic equations related with vortical motions, The Lond. Edinb. Dublin Philos. Mag. J. Sci. **33**, 485 (1867).

[4] D. Küchemann, Report on the IUTAM symposium on concentrated vortex motions in fluids, J. Fluid Mech. **21**, 1 (1965).

[5] Z.-S. She, E. Jackson, and S. A. Orszag, Intermittent vortex structures in homogeneous isotropic turbulence, Nature (London) **344**, 226 (1990).

[6] A. F. Hussain, Coherent structures-reality and myth, Phys. Fluids **26**, 2816 (1983).

[7] C. H. K. Williamson, Vortex dynamics in the cylinder wake, Annu. Rev. Fluid Mech. **28**, 477 (1996).

[8] Y. Dubief and F. Delcayre, On coherent-vortex identification in turbulence, J. Turbul. **1**, N11 (2000).

[9] J. C. Hunt, A. A. Wray, and P. Moin, Eddies, stream, and convergence zones in turbulent flows, in *Proceedings of the Summer Program* (Stanford University Center for Turbulence Research, Stanford, CA, 1988), N89-24555.
[10] J. Jeong and F. Hussain, On the identification of a vortex, J. Fluid Mech. **285**, 69 (1995).
[11] H. Wang, Q. Gao, and J. Wang, The statistical study of vortex structure in turbulent boundary layer flow based on Tomographic PIV, Sci. Sin. Phys. Mech. Astron. **45**, 124707 (2015).
[12] Z. Li, X.-W. Zhang, and F. He, Evaluation of vortex criteria by virtue of the quadruple decomposition of velocity gradient tensor, Acta Phys. Sin. **63**, 054704 (2014).
[13] C. Liu, Y. Gao, S. Tian, and X. Dong, Rortex—A new vortex vector definition and vorticity tensor and vector decompositions, Phys. Fluids **30**, 035103 (2018).
[14] Y. Wang, Y. Gao, and C. Liu, Galilean invariance of Rortex, Phys. Fluids **30**, 111701 (2018).
[15] Y. Gao, J. Liu, Y. Yu, and C. Liu, A Liutex based definition and identification of vortex core center lines, J. Hydrodyn. **31**, 445 (2019).
[16] T. Dairay, M. Obligado, and J. C. Vassilicos, Non-equilibrium scaling laws in axisymmetric turbulent wakes, J. Fluid Mech. **781**, 166 (2015).
[17] Y. Zhou and J. C. Vassilicos, Related self-similar statistics of the turbulent/non-turbulent interface and the turbulence dissipation, J. Fluid Mech. **821**, 440 (2017).
[18] Y. Zhou and J. C. Vassilicos, Energy cascade at the turbulent/nonturbulent interface, Phys. Rev. Fluids **5**, 064604 (2020)
[19] J. Nedić, J. C. Vassilicos, and B. Ganapathisubramani, Axisymmetric Turbulent Wakes with New Nonequilibrium Similarity Scalings, Phys. Rev. Lett. **111**, 144503 (2013).
[20] Y. Motoori and S. Goto, Generation mechanism of a hierarchy of vortices in a turbulent boundary layer, J. Fluid Mech. **865**, 1085 (2019).
[21] C. Liu, Y. Wang, Y. Yang, and Z. Duan, New omega vortex identification method, Sci. China Phys. Mech. Astron. **59**, 684711 (2016).
[22] C. Liu, Y. Gao, X. Dong, Y. Wang, J. Liu, Y. Zhang, X. Cai, and N. Gui, Third generation of vortex identification methods: Omega and Liutex/Rortex based systems, J. Hydrodyn. **31**, 205 (2019).
[23] S. Laizet and E. Lamballais, High-order compact schemes for incompressible flows: A simple and efficient method with quasi-spectral accuracy, J. Comput. Phys. **228**, 5989-6015 (2009).
[24] S. Laizet, E. Lamballais, and J. C. Vassilicos, A numerical strategy to combine high-order schemes, complex geometry and parallel computing for high resolution DNS of fractal generated turbulence, Comput. Fluids **39**, 471 (2010).
[25] D. K. Bisset, J. C. R. Hunt, and M. M. Rogers, The turbulent/non-turbulent interface bounding a far wake, J. Fluid Mech. **451**, 383 (2002).
[26] T. Watanabe, Y. Sakai, K. Nagata, Y. Ito, and T. Hayase, Wavelet analysis of coherent vorticity near the turbulent/non-turbulent interface in a turbulent planar jet, Phys. Fluids **26**, 095105 (2014).
[27] C. B. da Silva, R. R. Taveira, and G. Borrell, Characteristics of the turbulent/non-turbulent interface in boundary layers, jets and shear-free turbulence, J. Phys.: Conf. Ser. **506**, 012015 (2014).
[28] Y. Zhou, K. Nagata, Y. Sakai, H. Suzuki, Y. Ito, O. Terashima, and T. Hayase, Development of turbulence behind the single square grid, Phys. Fluids **26**, 045102 (2014).
[29] X. Dong, Y. Wang, X. Chen, Y. Dong, Y. Zhang, and C. Liu, Determination of epsilon for Omega vortex identification method, J. Hydrodyn. **30**, 541 (2018).
[30] Y. Wang, Y. Gao, J. Liu, and C. Liu, Explicit formula for the Liutex vector and physical meaning of vorticity based on the Liutex-Shear decomposition, J. Hydrodyn. **31**, 464 (2019).
[31] C. B. da Silva, J. C. R. Hunt, I. Eames, and J. Westerweel, Interfacial layers between regions of different turbulence intensity, Annu. Rev. Fluid Mech. **46**, 567 (2014).
[32] M. van Reeuwijk and M. Holzner. The turbulence boundary of a temporal jet, J. Fluid Mech. **739**, 254 (2014).
[33] G. Balamurugan, A. Rodda, J. Philip, and A. C. Mandal, Characteristics of the turbulent non-turbulent interface in a spatially evolving turbulent mixing layer, J. Fluid Mech. **894**, A4 (2020).
[34] R. R. Taveira and C. B. da Silva, Characteristics of the viscous superlayer in shear free turbulence and in planar turbulent jets, Phys. Fluids **26**, 021702 (2014).

[35] T. Watanabe, K. Nagata, and C. B. da Silva, *Vortex Sturucture in Fluid Dynamic Problems* (InTech, London, 2017).
[36] X. Dong, Y. Gao, and C. Liu, New normalized Rortex/vortex identification method, Phys. Fluids **31**, 011701 (2019).
[37] J. M. Wallace, Quadrant analysis in turbulence research: History and evolution, Annu. Rev. Fluid Mech. **48**, 131 (2016).
[38] S. K. Robinson, *Kinematics of Turbulent Broundary Layers Structure* NASA Tech. Memo. 103859 (NASA Ames Res. Cent., Moffett Field, CA, 1991).
[39] G. I. Park, J. M. Wallace, X. Wu, and P. Moin, Boundary layer turbulence in transitional and developed states, Phys. Fluids **24**, 035105 (2012).
[40] J. Jeong, F. Hussain, W. Shoppa, and J. Kim, Coherent structures near the wall in a turbulent channel flow, J. Fluid Mech. **332**, 185 (1997).
[41] J. Kim, P. Moin, and R. Moser, Turbulence statistics in fully developed channel flow at low Reynolds number, J. Fluid Mech. **177**, 133 (1987).
[42] J. M. Wallace, R. S. Brodkey, and H. Eckelmann, The wall region in turbulent shear flow, J. Fluid Mech. **54**, 39 (1972).
[43] C. B. da Silva and R. R. Taveira, The thickness of the turbulent/nonturbulent interface is equal to the radius of the large vorticity structures near the edge of the shear layer, Phys. Fluids **22**, 121702 (2010).
[44] C. B. da Silva and R. J. N. dos Reis, The role of coherent vortices near the turbulent/non-turbulent interface in a planar jet, Philos. Trans. R. Soc. A **369**, 738 (2011).
[45] T. Watanabe, J. J. Riley, K. Nagata, R. Onishi, and K. Matsuda, A localized turbulent mixing layer in a uniformly stratified environment, J. Fluid Mech. **849**, 245 (2018).
[46] M. Hayashi, T. Watanabe, and K. Nagata, The relation between shearing motions and the turbulent/non-turbulent interface in a turbulent planar jet, Phys. Fluids **33**, 055126 (2021).
[47] J. C. Vassilicos, Dissipation in turbulent flows, Annu. Rev. Fluid Mech. **47**, 95 (2015).
[48] J. C. Vassilicos, Beyond scale-by-scale equilibrium, Atmosphere **14**, 736 (2023).
[49] S. Tian, Y. Gao, X. Dong, and C. Liu, A definition of vortex vector and vortex, J. Fluid Mech. **849**, 312 (2018).
[50] A. Katz, *Computational Rigid Vehicle Dynamics* (Krieger Publishing Co., Malabar, FL, 1996).